Acta Materialia xxx (xxxx) 119654

Contents lists available at ScienceDirect

Acta Materialia

journal homepage: www.elsevier.com/locate/actamat

Demonstration of Helide formation for fusion structural materials as natural lattice sinks for helium

So Yeon Kim [a], Sina Kavak [b], Kübra Gürcan Bayrak [c], Cheng Sun [d], Haowei Xu [e], Myeong Jun Lee [f], Di Chen [g], Yong Zhang [a], Emre Tekoğlu [e], Duygu Ağaoğulları [b, h], Erhan Ayas [c], Eun Soo Park [f], Ju Li [a, e, *]

[a] Department of Materials Science and Engineering, Massachusetts Institute of Technology, Cambridge, MA, 02139, USA
[b] Particulate Materials Laboratories, Metallurgical and Materials Engineering Department, Istanbul Technical University, Maslak, Istanbul, 34469, Turkey
[c] Department of Materials Science and Engineering, Eskişehir Technical University, İki Eylül Campus, Eskişehir, 26555, Turkey
[d] Characterization and Advanced PIE Division, Idaho National Laboratory, Idaho Falls, ID, 83415, USA
[e] Department of Nuclear Science and Engineering, Massachusetts Institute of Technology, Cambridge, MA, 02139, USA
[f] Department of Materials Science and Engineering, Research Institute of Advanced Materials & Institute of Engineering Research, Seoul National University, Seoul, 08826, Republic of Korea
[g] Department of Physics and Texas Center for Superconductivity, University of Houston, Houston, TX, 77204, USA
[h] Istanbul Technical University, Prof. Dr. Adnan Tekin Materials Science and Production Technologies Applied Research Center, Maslak, Istanbul, 34469, Turkey

ARTICLE INFO

Keywords:
Irradiation
Helium
Grain boundary embrittlement
Ab initio calculations
Grazing incidence XRD

ABSTRACT

Fusion power holds promise as an ultimate energy source. However, achieving true sustainability in fusion energy requires addressing the embrittlement of polycrystalline materials in fusion reactors caused by transmutation helium, which leads to premature failure, often within a year. Here we experimentally demonstrate that nanodispersoids with constitutional vacancy-like atomic-scale free volume can securely store helium, not only at the matrix-dispersoid interface but also within their bulk lattices, which suggests their effectiveness in delaying critical helium damage of the polycrystalline matrix. The selected model nano-heterophase, fayalite Fe_2SiO_4, possesses moderately strong lattice sinks for helium while undergoing lattice distortions upon helium absorption. These distortions cause observable changes in peak intensities of X-ray diffraction (XRD) patterns, distinct from changes resulting from other factors like radiation damage. By comparing grazing incidence XRD patterns with *ab initio* computed patterns, we show that such nano-heterophases can store up to ~10 at% helium within their bulk lattice, forming a "helide compound." Incorporating just 1 vol% of Fe_2SiO_4 reduces helium bubble size and number density by >20 % and >50 %, respectively. These findings suggest that 1–2 vol% of appropriate ceramic nano-heterophases can accommodate a few thousand appm of bulk helium, expected to be generated over a 10-year operational period.

1. Introduction

Nuclear fusion is a highly sought-after energy source due to its potential for clean, abundant energy production. The technology required to harness this energy is, however, closely tied to the availability of materials that can withstand extreme conditions of radiation, high-temperature corrosion, and transient stresses [1]. For practical applications, fusion structural materials should withstand radiation damage of a few hundred displacements per atom (dpa) and helium concentrations of a few thousand appm at temperatures up to 1000 °C [2]. However, at such high temperatures, transmutation product gas helium (He) can diffuse and segregate readily at grain boundaries (GBs) [3], which have a larger free volume than in the lattice, as helium interacts with matrix atoms repulsively due to its electronically closed shell [4]. Two-dimensional (2D) GBs are particularly susceptible to such noble-gas segregation and resultant 2D interfacial debonding [4], since the stress amplification factor for a penny-shaped opening leads to tensile stress singularity when the long-to-short axis ratio approaches infinity [5]. This makes catastrophic autocatalytic failures possible, especially considering that GBs in polycrystalline engineering materials form a percolating network, thus facilitating macroscopically percolating long cracks. Consequently, even a minute quantity of helium (e.g., as low as

* Corresponding author.
E-mail address: liju@mit.edu (J. Li).

https://doi.org/10.1016/j.actamat.2024.119654
Received 29 October 2023; Received in revised form 23 December 2023; Accepted 4 January 2024
1359-6454/

100 appm in a 5 μm grain-sized polycrystal) can significantly compromise the mechanical integrity of the polycrystalline engineering material due to its interfacial segregation within the percolating 2D GB network. [6].

"0D" or "1D" nano-heterophases have garnered attention due to their potential to enhance not only the high-temperature creep resistance [7,8] and radiation resistance [9,10] but also helium tolerance [11,12]. Particularly noteworthy are nano-oxide dispersion-strengthened (NODS) steels, such as nanostructured ferritic alloys (NFAs) and nanostructured tempered martensitic steels (NMS). These materials feature an exceptionally high density of ultrafine (2–3 nm) Y-*M*-O (*M* = Ti, Zr, Hf, etc.) nano-oxides, which enable impressive helium tolerance by confining helium within small nanometer-scale *interfacial* bubbles [13–15]. These nano-heterophase interfaces are expected to be less damaging even when fully debonded, as "0D" spherical or "1D" prolate/needle-like cavities avoid stress singularity that occurs in "2D" oblate cavity or penny-crack type openings under a far-field stress [4]. This point is well illustrated by Fig. 2 of Nabarro's paper [5], where extreme oblateness ("2D") gives rise to catastrophic elastic softening that is characteristic of a cracked material.

Theoretical hypotheses have been proposed regarding the involvement of nano-oxides in the early stages of helium sequestration. First-principles calculations indicate that helium is initially confined within the *interior* of nano-oxides but generates *interfacial* bubbles as they grow to a size where the chemical potential of helium becomes lower within the phase boundary (PB) than within the nano-oxides [16–18]. This theoretical framework suggests that if the *bulk lattice* of the nano-heterophase possesses a helium embedding energy significantly lower than that of GBs and PBs, enabling it to absorb and store helium up to ~10 at%, then the composite can endure helium concentrations of a few thousand appm(He) [4,8]. Based on this theoretical foundation, other nano-heterophases, such as early transition metal carbonitrides featuring constitutional vacancies [12,19] or phases with large atomic-scale free volume [4], are currently under investigation. These investigations complement the study of Y-*M*-O pyrochlore and aim to enhance manufacturability and facilitate the development of helium-tolerant alloys with different base metals, thereby expanding the operating temperature range.

However, experimental demonstration of atomic helium storage within the *lattice interior* of nano-heterophases upon irradiation—formation of "helide" (i.e., similar to noble gas-containing inorganic clathrates [20–22])—is still lacking. Transmission electron microscopy has been successful in achieving atomic resolution but still entails the overlap of atoms, making it difficult to pinpoint where helium resides [12]. Probing helium atoms via atom probe tomography is challenging and requires careful experimentation and analysis due to many factors, including the high ionization energy of helium [23], its inert nature [24], mass spectra overlap [25], and the possibility of outgassing from nanometer-thick specimens [26]. X-ray diffraction and Raman scattering can detect changes in lattice constants or vibrational modes resulting from helium absorption, but most of the demonstrations were carried out under GPa-level pressure [27–30].

In this study, via the combined approach of experiments and computation, we demonstrate that phases with moderately large atomic-scale free volume can store helium within their *lattice*, essentially forming a helide compound. We employed a combination of *ab initio* calculations and grazing incidence X-ray diffraction (GIXRD) using iron (Fe) as the model matrix and fayalite (Fe_2SiO_4) as the model helium-absorbing nano-heterophase. Fayalite (Fe_2SiO_4) is a moderately strong lattice sink for helium that offers a helium embedding energy lower than that of GBs in BCC Fe by ~3 eV (equivalent to tens of GPa hydrostatic pressure) according to our density functional theory (DFT) calculations. The absorption of helium in a confined volume can result in lattice distortions that manifest changes in the width of diffraction peaks, some of which even sharpen, making them distinguishable from the effect of general radiation damage. We thus injected helium ions into a metal-matrix composite containing finely dispersed nanoscale Fe_2SiO_4 and analyzed the changes in its GIXRD patterns indicative of helide formation by lattice helium absorption. The experimental patterns showed good agreement with *ab initio* computed XRD patterns of Fe_2SiO_4·He, implying that such nano-heterophase can store helium up to ~10 at% within its bulk lattice. We also found that the incorporation of 1 vol% Fe_2SiO_4 reduced helium bubble size and number density in the matrix by > 20 % and > 50 % respectively. This finding enables quantification of the volume fraction of nano-heterophases necessary to safely accommodate a few thousand appm(He), satisfying the requirements for fusion power plants.

2. Methods

2.1. Ab initio calculations for designing potential helide formers

Ab initio calculations were conducted to determine the helium embedding energies of various crystal structures, and to generate theoretical X-ray diffraction (XRD) patterns for crystal structures with and without embedded helium. The Vienna Ab initio Simulation Package (VASP) [31], operating on density functional theory (DFT) principles [32,33], was utilized for *ab initio* calculations. Crystallographic Information Framework (CIF) files were downloaded from the Materials Project database [34]. The crystallographic positions for helium embedding were determined based on atomic-scale free volume, quantified by the maximum sphere radius that can fit within the crystal structure without introducing defects (denoted as r_{max}). The Atomic Simulation Environment (ASE) package was used to calculate r_{max}; each atom in the host material was considered as a sphere with a radius corresponding to its covalent radius, following Ref. [4], due to the challenges associated with accurately incorporating the dependence on coordination numbers when considering the ionic radius. Positions with r_{max} were identified using the PLATON software [35]. Generalized gradient approximation (GGA) in the form of Perdew-Burke-Ernzerhof (PBE) functional [36] was employed to account for exchange-correlation interactions. The projector augmented wave (PAW) method [37] was employed to handle both core and valence electrons, while plane-wave basis functions were used. Supercells with dimensions exceeding 10 Å were constructed, and the first Brillouin zone was sampled using a 3 × 3 × 3 ***k***-mesh. During the relaxation of the atomic structure, the forces acting on each atom were minimized below 5×10^{-3} eV/Å, while maintaining the shape and volume of the crystal. The relaxed atomic structures were then utilized to compute the theoretical XRD patterns using a 3D visualization program called VESTA [38]. The computed XRD patterns were based on a wavelength of 0.692649 Å, corresponding to the X-ray source employed in the grazing incidence XRD experiment described later. K_β peaks were excluded from the analysis.

2.2. Thermodynamic calculations and materials synthesis

To synthesize composites containing Fe_2SiO_4, temperature-dependent Fe-Si-O ternary phase diagrams were analyzed using the CALculation of PHAse Diagrams (CALPHAD) in combination with the Thermo-Calc software and TCFE8 database. As Fe powders can introduce excess oxygen, SiO_2 nanopowders, commercially available with a particle size of 10–20 nm, were added to Fe instead of Fe_2SiO_4, up to a volume fraction of 2 %. Fe powders with a particle size of 5–9 μm with 99.9 % purity were supplied from STREM, and SiO_2 nanopowders with 99.5 % purity were supplied from SkySpring Nanomaterials. The prepared powders were transferred to stainless steel vials (50 ml) containing stainless steel balls (ϕ 6 mm) in Ar atmosphere (Linde, 99.999 % purity) within a glovebox (MBRAUN). The powders in 15 g batches were then high-energy ball milled using a SPEX™ 8000D Mixer/Mill at 1200

rpm for 4 hr. The milling operation was halted for 30 min at intervals to prevent overheating. For all the milling experiments, the ball-to-powder weight ratio was kept at 7:1. In addition, 4 hr-milled Fe powders were also prepared using the same method for comparison purposes. The powders were sintered utilizing a spark plasma sintering system (FCT HP D 25/I, FCT System GmbH). The sintering experiments were conducted under a vacuum of 10^{-2} mbar with a heating rate of 100 °C/min, a dwell time of 5 min, and an axial pressure of 65 MPa. To prevent any polymorphic phase transformation of SiO_2 that could affect the sintering experiments, the sintering temperature was set at 800 °C. The temperature, pressure, and ram displacement were recorded as a function of time throughout the sintering process.

2.3. Design of helium ion implantation and grazing incidence X-ray diffraction experiments

For helium ion implantation, bulk materials were first cut into 5 mm × 5 mm square specimens. These specimens were then ground to a thickness of 1 mm and subsequently polished using polishing fluids containing particles as small as 0.05 μm. To achieve a Fe_2SiO_4-to-helium ratio close to 1:1 within the volume probed by GIXRD, the energy and the fluence of helium ions were set to 800 keV (based on the projected ranges shown in Fig. 1a) and 9.6 × 10^{15} cm^{-2}, respectively. The Stopping and Range of Ions in Matter (SRIM) simulation, employing the Kinchin-Pease approximation [39,40], predicts a maximum helium concentration at a depth of around 1.4 μm under these conditions, reaching 5000 appm(He) locally (Fig. 1b). The corresponding maximum radiation damage is estimated to be ~0.21 dpa. To prevent helium loss due to outgassing and maintain a unimodal distribution, the ion implantation temperature was set at 500 °C [3,41].

To investigate the structural changes induced by helium ion implantation, particularly within the few-micron region near the surface, GIXRD experiments were conducted at the 5A-XRS beamline of the Pohang Light Source, located at the Pohang Accelerator Laboratory in South Korea. A monochromatic X-ray beam with a wavelength of 0.692649 Å (equivalent to 17.8 keV) was utilized in a reflection mode. The incident angle was set at 1° to achieve a Fe_2SiO_4-to-helium ratio close to 1:1 within the X-ray probed volume based on X-ray attenuation lengths at different angles, which were estimated using an X-ray attenuation length calculator provided by Lawrence Berkeley National Laboratory (https://henke.lbl.gov/optical_constants/atten2.html). The resulting X-ray penetration depths were calculated based on the Beer-Lambert law and are summarized in Fig. 2a. For instance, at an incident angle of 1°, the X-ray attenuation length is estimated to be 0.65 μm. Consequently, the relative intensity of X-ray (I_s/I_0, where I_s and I_0 represent the intensities of the scattered and incident X-rays, respectively) from the sample volume deeper than 1.5 μm would be less than 1 % under the given experimental conditions. Only half of the square specimens (2.5 mm × 5 mm) were subjected to ion implantation, and grazing incidence XRD experiments were performed on each side of the square specimens, as depicted in Fig. 2b, to compare the effect of he-

a

Ion energy (keV)	Projected range (μm)
400	0.81
500	0.95
600	1.09
700	1.22
800	1.36
900	1.49
1000	1.63
1100	1.77
1200	1.91

b

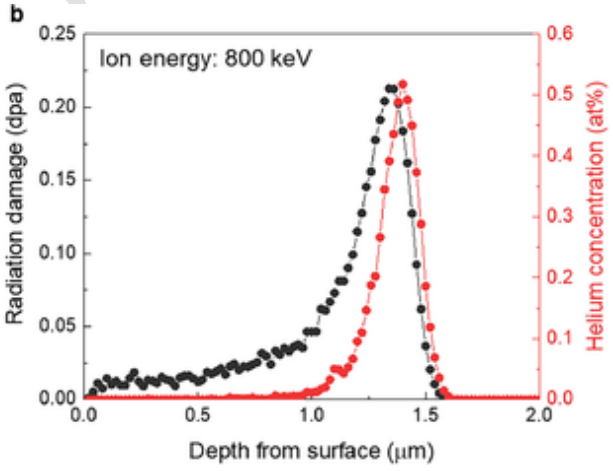

Fig. 1. Stopping and Range of Ions in Matter (SRIM) calculation results used to determine the appropriate experimental parameters for helium ion implantation. (a) Summary of helium ion energy and its corresponding projected range of ions. (b) Plot of radiation damage and helium concentration as a function of depth from the surface. The ion energy used was 800 keV.

a

Incident angle (°)	Penetration depth (μm)
0.5	0.7
1.0	1.5
1.5	2.2
2.0	3.0
2.5	3.7
3.0	4.5

b

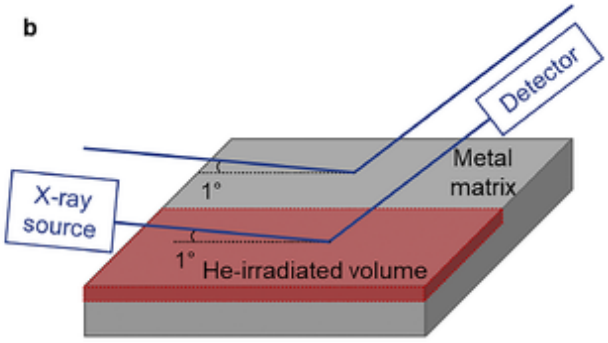

Fig. 2. Experimental conditions for grazing incidence X-ray diffraction. (a) Summary of incident angle and its corresponding penetration depth. The penetration depth was defined as the depth at which the relative intensity of X-ray (I_s/I_0, where I_s and I_0 are the intensities of the scattered and the incident X-rays, respectively) falls to 1 %. (b) Schematic diagram of the setup for grazing incidence X-ray diffraction experiments. The incident X-ray was directed at an angle of 1° to achieve a Fe_2SiO_4-to-helium ratio close to 1:1.

lium embedding on the crystal structures while minimizing the influence of other factors.

2.4. Microstructural characterization

2.4.1. Electron microscopy

The microstructure of the alloys was examined using a Zeiss Merlin High-Resolution Scanning Electron Microscope (SEM) equipped with an energy-dispersive spectrometer (EDS) and a JEOL 2010 FEG Analytical Transmission Electron Microscope (TEM) operating at 200 kV. The TEM analysis involved energy-dispersive spectroscopy with the Oxford AZtec microanalysis system and electron energy loss spectroscopy (EELS) using the Gatan Image Filter (GIF 200). TEM specimens were prepared using an FEI Helios Nanolab 600 Dual Beam System, and their thickness was determined using low-loss EELS spectra through the log-ratio method [42].

To visualize helium bubbles, a negative defocus was employed to generate Fresnel fringe contrast around the bubbles. The MIPAR Image Analysis software was utilized to detect helium bubbles from the TEM images. As it is challenging to differentiate Fe_2SiO_4 particles with an equivalent diameter on the order of 10 nm from helium bubbles solely based on EDS maps, point EDS analyses were conducted for such small features. The matrix oxygen content, as measured by scanning transmission electron microscopy (STEM)-EDS, does not exceed ~7 at%. Consequently, features exhibiting an oxygen content greater than 7 at% were classified as oxide particles, with the minimum observed oxygen content among these features being 8.2 at%. Bubbles attached to the oxide particles were excluded from the quantitative analysis conducted on the bubbles within the matrix.

2.4.2. High-energy X-ray diffraction

To quantify the fraction of different phases, high-energy X-ray diffraction experiments were performed at the 11-ID-C beamline of the Advanced Photon Source, located at Argonne National Laboratory in the USA. A high-energy monochromatic X-ray beam with a wavelength of 0.1173 Å was employed in the transmission state. The incident beam dimension was 500 μm × 500 μm, and the diffracted beam was recorded using a two-dimensional large-area detector (PerkinElmer) with a quadratic pixel size of 200 μm × 200 μm, positioned behind the sample at a distance of ~1500 mm. The instrument parameters were calibrated using standard CeO_2 powder. Rietveld refinement of the recorded ring patterns was carried out using the Material Analysis Using Diffraction (MAUD) software [43]. The recorded ring patterns were integrated over 5° of azimuth angles and converted into 72 1-D patterns. These converted patterns were simultaneously analyzed following the instructions provided in the appendix of Ref. [44]. Line broadening, size-strain, and texture models were implemented using the Delft, isotropic, and E-WIMV algorithms, respectively. The lattice parameters of Fe_xO and Fe_2SiO_4 used for the Rietveld refinement are listed in Table S1. The initial crystal structure used for fitting the ring patterns of Fe_xO was the stoichiometric compound mp-1279,742 from the Materials Project database [34].

3. Results and discussion

3.1. Model material design: potential helide formers and fabrication of a composite incorporating them

Fig. 3 illustrates the suitability of fayalite Fe_2SiO_4 as a model phase for demonstrating the formation of a helide compound from multiple factors including helium-absorbing potency and structural changes associated with helium absorption. First, the helium-absorbing potency can be assessed by considering the helium embedding energy ($\mathscr{E}_{emb}$), and atomic-scale free volume characterized by the radius of the largest sphere that can be fitted in the crystal structure without any defects (r_{max}) is an easy-to-compute metric for low $\mathscr{E}_{emb}$ [4]. The r_{max} and $\mathscr{E}_{emb}$ of fayalite Fe_2SiO_4 (mp-20,313 in Materials Project database [34]) are calculated to be 1.15 Å and 0.65 eV/He, respectively, whereas $\mathscr{E}_{emb}$ of GBs in BCC Fe is on the order of 4 eV/He [4]. Considering the van der Waals excluded volume (b) of a single helium atom [45] (23 Å^3 per atom = 0.144 eV/GPa), which corrects the ideal gas law for finite atomic or molecular sizes, a $\Delta\mathscr{E}_{emb}$ of >3 eV/He can in principle provide a hydrostatic pressure greater than 20 GPa, which is comparable to that required to insert helium into clathrates in high-pressure diffraction experiments [46,47]. Fe_2SiO_4 is thus expected to be capable of storing helium in its bulk lattice at a lower energy cost than the GBs of BCC Fe, thereby driving the diversion of helium towards its atomic-scale free volume. Fig. 3a shows the crystal structure of fayalite Fe_2SiO_4; beige spheres represent positions where r_{max} >1 Å. Four inequivalent loca-

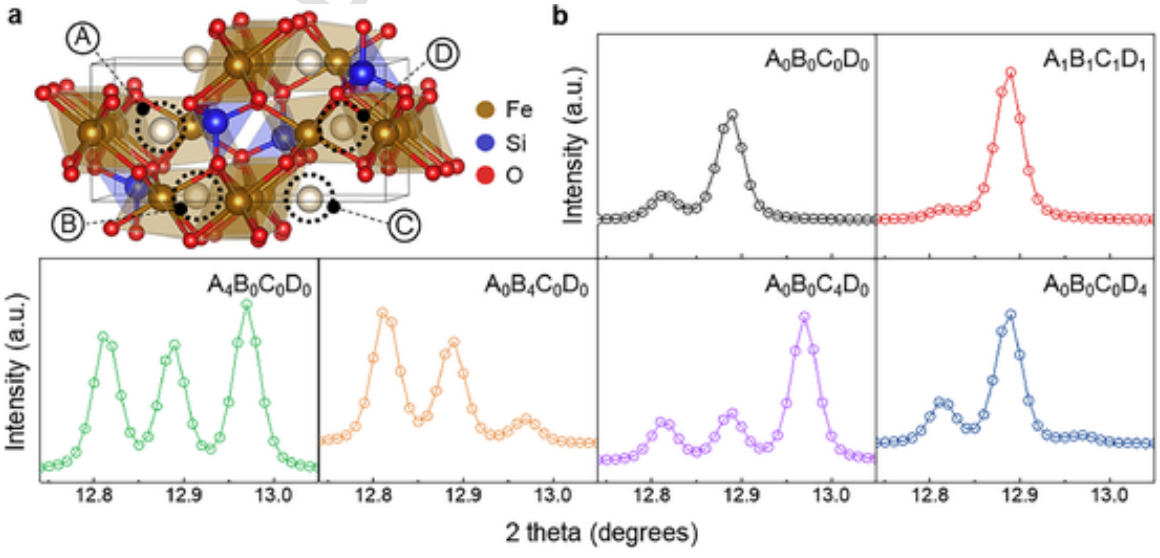

Fig. 3. Potential helide formers. (a) Crystal structure of fayalite Fe_2SiO_4. Beige spheres indicate positions where atomic-scale free volume (r_{max}) is greater than 1 Å. Four inequivalent locations of cage-like atomic-scale free volume are labeled as A, B, C, and D, respectively. (b) Ab initio computed XRD patterns of Fe_2SiO_4 with or without helium atoms. The X-ray wavelength used is 0.692649 Å, and K_β peaks are neglected. Subscripts in $A_xB_yC_zD_w$ indicate the number of helium atoms in each cage.

tions of cage-like atomic-scale free volume exist in Fe_2SiO_4 and are labeled as A, B, C, and D, respectively.

Second, the storage of helium within its atomic-scale free volume leads to changes in the relative intensities of the XRD peaks, which can be distinguished from the effects of radiation damage. Fig. 3b presents the varying relative intensities of the *ab initio* computed XRD peaks, reflecting the positions of the inserted helium atoms in relation to the cages. For example, when no helium atoms are present ($A_0B_0C_0D_0$), two peaks corresponding to {322} and {040} planes appear at 12.81° and 12.89°, respectively. When four helium atoms are uniformly distributed over different cages ($A_1B_1C_1D_1$), the first peak almost disappears, while the second peak sharpens. On the other hand, when all four helium atoms are stored in cage A ($A_4B_0C_0D_0$), an additional peak corresponding to {023} becomes apparent at 12.97°, in addition to the two peaks observed in the earlier cases. Depending on which cage the four helium atoms occupy, the relative intensities of these three peaks change. Although radiation knock-out of atoms, measured in units of displacements per atom (dpa), is inevitable in fusion structural materials, it is more likely to broaden peaks rather than sharpen them as it introduces additional scattering centers [48]. Therefore, changes in XRD peak intensities could serve as definitive evidence of helium storage within the lattice of the nano-heterophases.

Furthermore, such nanoscale Fe_2SiO_4 phases can be introduced simply by adding SiO_2 nanoparticles to Fe via conventional powder metallurgy processing. Commercial Fe powders tend to have excess oxygen content, which increases the oxygen-to-silicon ratio (c_O/c_{Si} in at%). By adopting an oxygen-rich regime ($c_O/c_{Si} > 4$), a Fe-Fe_xO-Fe_2SiO_4 system can be compared with a Fe-Fe_xO system, as shown in the isothermal cross-section of the Fe-Si-O ternary phase diagram at 800 °C in Fig. 4.

Fig. 5a,b display the microstructures of two samples observed using a scanning electron microscope (SEM): one without Fe_2SiO_4 (S-0) and one with Fe_2SiO_4 (S-Fe_2SiO_4), respectively. Sub-micron scale dark phases are present in both samples, with S-Fe_2SiO_4 also exhibiting nanoparticles with diameters of a few tens of nanometers, corresponding to the size of the added SiO_2 nanoparticles. Fig. 5c,d show the spatial distribution of oxygen and silicon suggesting that the sub-micron scale dark phases are oxides with little to no silicon content. High-energy X-ray diffraction (HEXRD) results suggest that S-0 comprises BCC Fe and 3.7 vol% of Fe_xO, whereas S-Fe_2SiO_4 comprises BCC Fe, 3 vol% of Fe_xO, and 1 vol% of Fe_2SiO_4 (Fig. 3e). Fe_xO is referred to as FeO here for simplicity. As the volume fraction of FeO is comparable in both samples, it is assumed that the effect of FeO is negligible. Detailed analyses of particle density and particle size can be found in Fig. S1. Given a volume fraction (V_f) of 1 vol% and an average radius (r) of 14 nm for Fe_2SiO_4, interparticle spacing ($l = r\sqrt{\pi/V_f}$) is estimated to be ~250 nm. This spacing is approximately half the size of the matrix grains of S-Fe_2SiO_4, which enables the absorption of helium from the Fe matrix. Considering the $\mathscr{E}_{emb}$ of Fe grain boundaries and Fe_2SiO_4, which are lower than that of the matrix by ~1 eV at the largest and ~3 eV, respectively, the pressure gradient would be sharper towards Fe_2SiO_4 unless helium is three times closer to the grain boundaries. This situation would drive the diversion of helium towards Fe_2SiO_4.

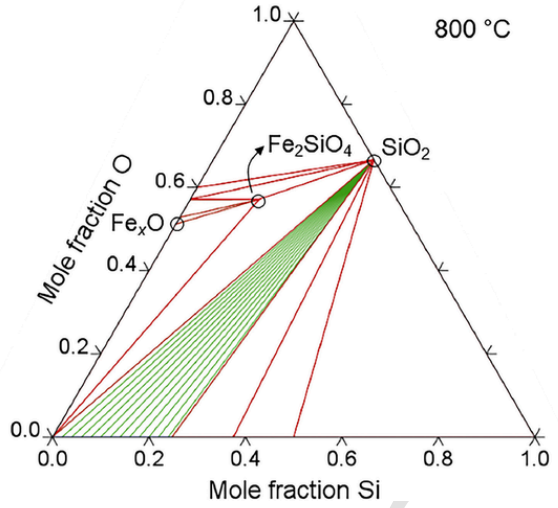

Fig. 4. Isothermal cross-section of Fe-Si-O ternary phase diagram at 800 °C.

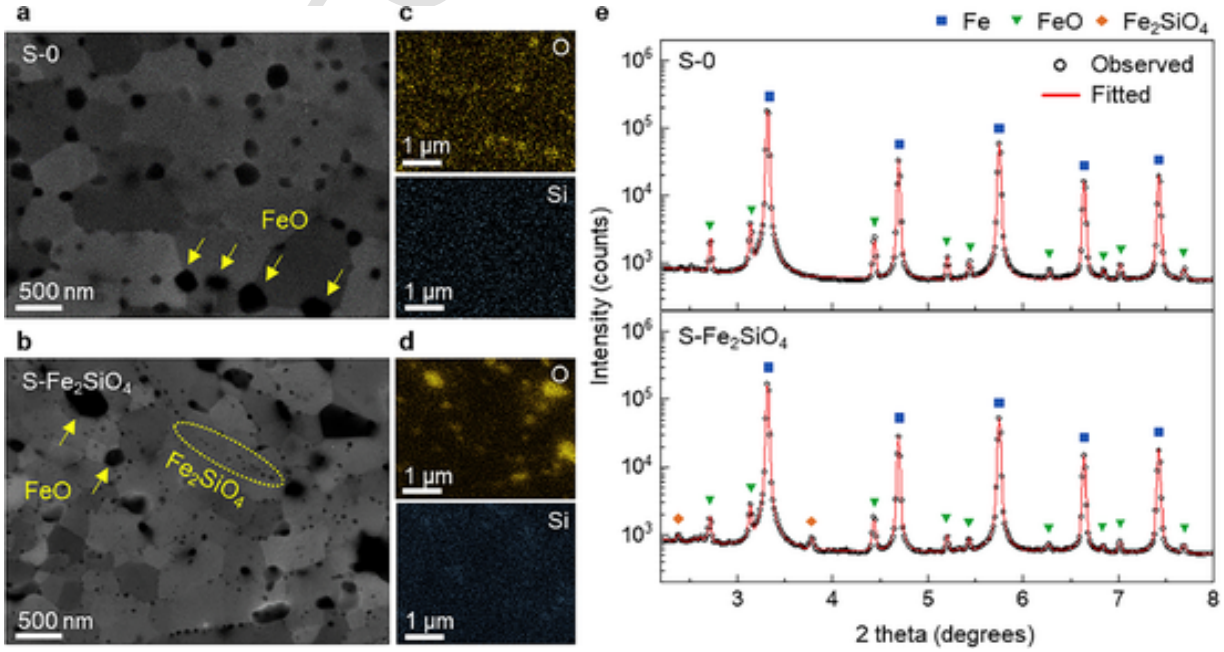

Fig. 5. Microstructure of as-fabricated composites. (a,b) SEM micrographs of (a) S-0 and (b) S-Fe_2SiO_4. A few FeO and Fe_2SiO_4 particles are marked as an example. (c,d) EDS maps (oxygen and silicon) of (c) the region corresponding to (a) and (d) the region corresponding to (b). (e) High-energy XRD patterns of S-0 and S-Fe_2SiO_4. The X-ray wavelength used is 0.1173 Å.

3.2. Proof of principle: experimental validation of helium storage within the lattice interior of helide formers

Based on Fig. 5, we proceed to investigate where Fe_2SiO_4 stores helium (particularly, whether it stores helium in its lattice interior or not) via helium ion implantation and grazing incidence X-ray diffraction (GIXRD). To achieve a Fe_2SiO_4-to-helium ratio close to 1:1 for comparison with *ab initio* computed XRD patterns, helium ion implantation was performed using 800 keV helium ions up to a fluence of 9.6×10^{15} /cm^2, and the incident angle of the X-ray was set at 1°, as described in Methods. The temperature used was 500 °C, which is below half of the melting temperature of Fe ($T_M/2$ = 905 K ~632 °C), above which helium embrittlement becomes more severe [3]. However, it is still high enough for helium atoms to diffuse and form bubbles, while being low enough to prevent helium loss due to outgassing and maintain unimodal distribution [3,41].

The GIXRD patterns of S-0 and S-Fe_2SiO_4 exhibited differences in the magnitude of changes in interplanar spacing, suggesting the potential storage of a substantial fraction of injected helium atoms within the oxide phases, unless they are subsequently outgassed. Fig. 6 shows the main GIXRD peaks of Fe and FeO in S-0 before (gray) and after (pink) helium irradiation. In S-0 (Fig. 6a), the peaks of Fe and FeO were positively shifted (0.14% and 0.05 % decrease in terms of interplanar spacing, respectively), suggesting the presence of a compressive stress field. This is probably because additional volumetric elements are introduced into a confined volume, forming bubbles within the matrix. Likewise, those of Fe and FeO are also positively shifted in S-Fe_2SiO_4 upon helium irradiation as shown in Fig. 6b (blue: before; red: after). However, the change was barely detectable with the current resolution, which was 0.02 % in terms of interplanar spacing. Moreover, no shift was observed for the main peaks of Fe_2SiO_4. Considering that the bulk modulus of Fe_2SiO_4 (~166 GPa) is similar to that of Fe (160–178 GPa), Fe_2SiO_4 is expected to experience a comparable level of compression in the presence of a compressive stress field. One potential explanation for the lesser degree of change observed in Fe_2SiO_4 could be the existence of a stress field that counteracts such compression, such as the opposing stress induced by the storage of helium within its atomic-scale free volume.

Despite the absence of a noticeable change in interplanar spacing, the storage of helium can still affect the crystallinity of Fe_2SiO_4. The implanted helium content within the probed sample volume using GIXRD is ~0.08 at%. If the outgassing had been the main cause of the difference in the peak shift between S-0 and S-Fe_2SiO_4, almost all helium atoms should have been outgassed. The grain size of S-Fe_2SiO_4 is smaller than S-0 (Fig. 5a,b), and thus, more helium atoms could have escaped, but outgassing of a majority of helium atoms is not likely at 500 °C [41]. We thus hypothesized that a significant portion of the ~0.08 at% helium is stored in Fe_2SiO_4. Considering that Fe_2SiO_4 accounts for ~0.1 mol % in the current composite, each Fe_2SiO_4 molecule should take up approximately 0.8 He (i.e., ~10 at%). Since the unit cell of Fe_2SiO_4 contains four Fe_2SiO_4 molecules, this corresponds to 3–4 helium atoms per Fe_2SiO_4 unit cell, which has four inequivalent locations for atomic-scale free volume or cages (Fig. 3a). If each cage is sufficiently large, storing none or one helium atom per cage may not cause the lattice to expand significantly, especially when the volume is confined, but it could lead to moderate distortion in the crystal lattice, which may manifest as a change in crystallinity.

To investigate this possibility, DFT calculations were used to compute theoretical XRD patterns, which were then compared with experimental XRD patterns. Fig. 7a displays the GIXRD patterns of four different samples: S-0 and S-Fe_2SiO_4 before and after helium irradiation. Peaks associated with Fe_2SiO_4 are labeled as P-1, P-2, P-3, and P-4. The absence of these peaks in the patterns of S-0 confirms that they originate from Fe_2SiO_4. Fig. 7b shows computed XRD patterns of Fe_2SiO_4 with and without helium atoms; for the former, one helium atom was inserted per cage for a total of four helium atoms per unit cell (Fe_2SiO_4·He). Although peak positions differ slightly from experimental XRD patterns, four distinct peaks that correspond to each peak labeled in experimental XRD patterns are observed.

The comparison of the changes in peak intensities resulting from the addition of helium between the experimental and computed patterns reveals a good agreement, providing compelling evidence for helium storage within the bulk lattice of Fe_2SiO_4. Specifically, both P-1 and P-4 decrease with the addition of helium atoms, with P-4 decreasing more than P-1 in both patterns. In addition, P-2 almost disappears with helium atoms, while P-3 sharpens in both cases. Since peak sharpening is less likely to occur as a result of radiation damage [48], this result confirms the presence of helium atoms within its lattice and the formation of a helide. Moreover, the complete disappearance of P-2 suggests that not only the near-surface lattice but also the center region of a few tens of nanometers-large Fe_2SiO_4 is accessible by helium atoms without major kinetic confinement. When helium atoms are uniformly distributed

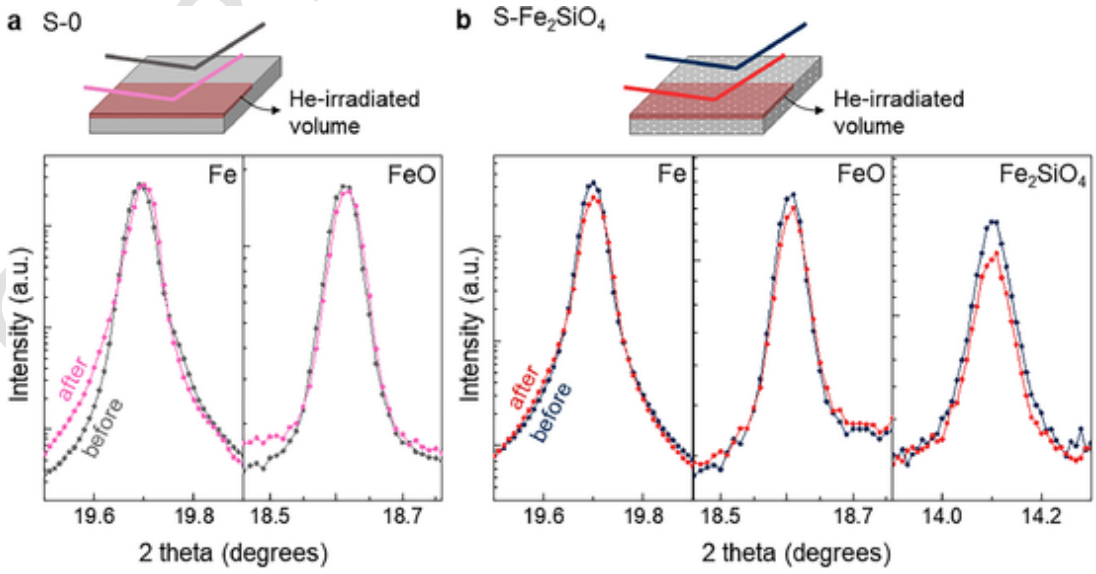

Fig. 6. Effect of helium irradiation on the crystal structure of the phases constituting the composites. (a,b) Grazing incidence XRD patterns of (a) S-0 and (b) S-Fe_2SiO_4 comparing the position of the main XRD peaks of Fe, FeO, and Fe_2SiO_4 before (gray and blue) and after (pink and red) helium irradiation.

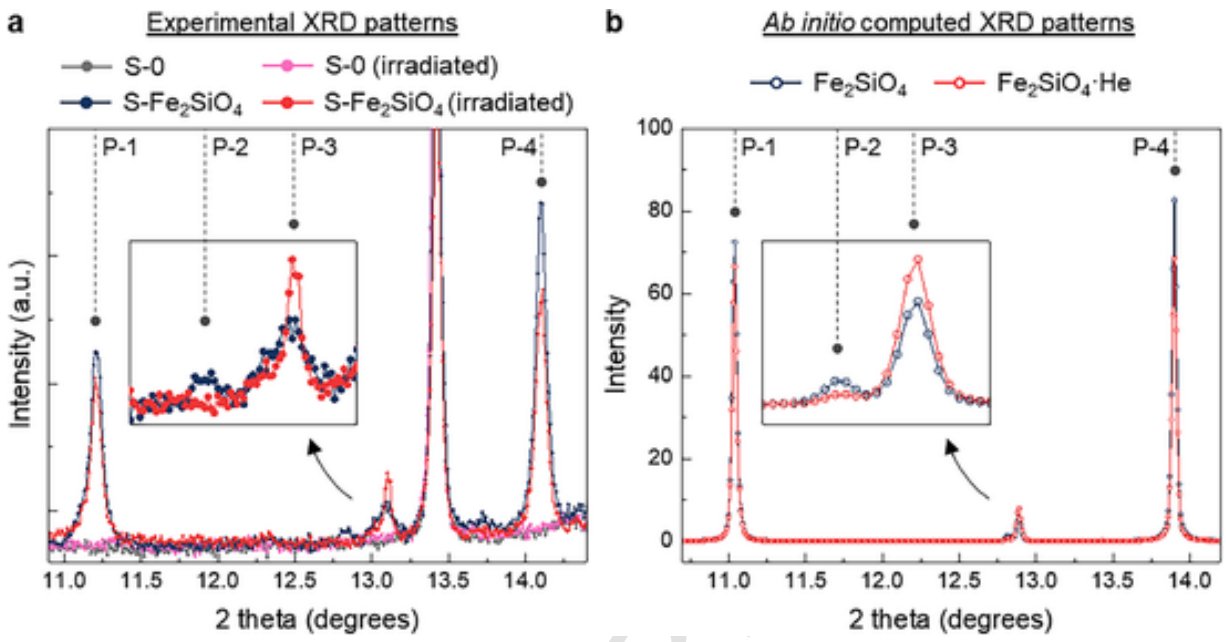

Fig. 7. Comparison of XRD patterns. (a) Experimentally measured grazing incidence XRD patterns of S-0 and S-Fe_2SiO_4 before and after helium irradiation. (b) Ab initio computed XRD patterns of Fe_2SiO_4 with and without helium atoms. For theoretical XRD patterns, one helium atom was inserted per cage, resulting in a total of four helium atoms per unit cell (Fe_2SiO_4·He). The change in shape and volume was not allowed, and the wavelength of 0.692649 Å, which is that of the X-ray source used for the experiment, was used with K_β peaks neglected.

over cages ($A_1B_1C_1D_1$), $\mathscr{E}_{emb}$ remains much smaller (~0.77 eV/He) than that of GBs in BCC Fe (~4 eV/He) [4]; thus, its full helium-absorbing capacity is expected to be greater than 10 at%.

3.3. *Property enhancement: helide formers-assisted suppression of helium gas bubbles*

To examine the effect of potential helide formers on the development of helium gas bubbles, transmission electron microscopy was performed on the regions of peak damage in the helium-irradiated samples, specifically near the depth of ~1.4 μm from the surface. Fig. 8 shows the microstructure of S-0 after helium irradiation observed using TEM. The under-focused images are shown to better visualize the helium bubbles. One can see a few submicron-sized (> 100 nm) particles, which are FeO phases. A few faceted helium bubbles formed inside these phases near their interface with the Fe matrix, but still, there are a large number of helium bubbles with a diameter of a few nanometers in the matrix. To further investigate the number density and size distribution of the helium bubbles, automated feature detection software was applied to process multiple TEM images for enhanced visualization of the helium. The regions investigated span over an area of 420 nm × 2 μm at a depth of approximately 1.4 μm. The average thickness of the S-0 TEM specimen measured via electron energy loss spectroscopy (EELS) is 89 nm. An example of this process is shown in Fig. 8b–e. Fig. 8c shows the image preprocessed to better detect helium bubbles corresponding to Fig. 8b. Since large features like the ones indicated by white arrows in Fig. 8c could be either large helium bubbles or small oxide phases, EDS mapping was performed in a scanning transmission electron microscopy (STEM) mode, as shown in Fig. 8d, to distinguish helium bubbles from oxide phases. Finally, Fig. 8e shows the result of bubble detection with bubbles being marked in red.

Likewise, the microstructure of S-Fe_2SiO_4 was investigated using the same methodology and parameters. In Fig. 9a, nanoparticles with a diameter of a few tens of nanometers, which are supposed to be Fe_2SiO_4, were additionally observed, as compared to S-0. To obtain better statistics, a larger region was explored for S-Fe_2SiO_4 than that for S-0. The region investigated spans over 420 nm × 5 μm, and the average thickness of the sample in this region measured via EELS is 98 nm. Fig. 9b–e display the results of preprocessing and helium bubble detection as well as STEM-EDS. The EDS map of Si is presented in Fig. 9d to clarify that the observed features are Fe_2SiO_4 rather than FeO, and the EDS map of O is provided in Fig. S2.

Meanwhile, distinguishing Fe_2SiO_4 particles with an equivalent diameter on the order of 10 nm from helium bubbles based on EDS maps is challenging. Bright-field TEM images at various tilt angles or dark-field TEM images can aid in distinguishing oxide particles from bubbles, as they provide contrast differences enabled by crystallinity. However, this approach is not universally applicable due to contrast originating from other factors, such as defects and bend contours. To address this issue, we adopted oxygen content as a practical criterion, which can be measured through point EDS analyses in a relatively high-throughput manner. More specifically, the oxygen content of the matrix, as measured by STEM-EDS, hardly exceeds ~7 at%. Therefore, features displaying an oxygen content greater than 7 at% were categorized as oxide particles, with the minimum oxygen content found among these features being 8.2 at%; the dark-field TEM image of the relevant feature is shown in Fig. S2. In our study, only a few bubbles grew to the size of ~10 nm, even in S-0 under the applied radiation dose. Moreover, atom probe measurements confirmed the presence of oxide particles with a diameter on the order of 10 nm in S-Fe_2SiO_4 (Fig. S3). Hence, it is likely that most of the features on this size regime with high oxygen content are oxide particles. However, it should be noted that this criterion may not be generally applicable, especially when the size range of bubbles and oxide particles heavily overlaps.

Fig. 10a,b present the processed images of helium-irradiated S-0 and S-Fe_2SiO_4, respectively. Helium bubbles are highlighted in red, and grain boundaries are indicated by white dotted lines; the TEM micrographs without red dots are provided in Fig. S5. A reduction in the volume of helium bubbles was observed in the peak damage region of S-Fe_2SiO_4 compared to S-0. In S-0, a few faceted helium bubbles were observed inside submicron-sized (> 100 nm) FeO phases, near their interface with the Fe matrix (Fig. 8a). Still, a large portion of helium bubbles with a diameter of a few nanometers were in the matrix, with some segregating along GBs, as depicted in Fig. 10a. A

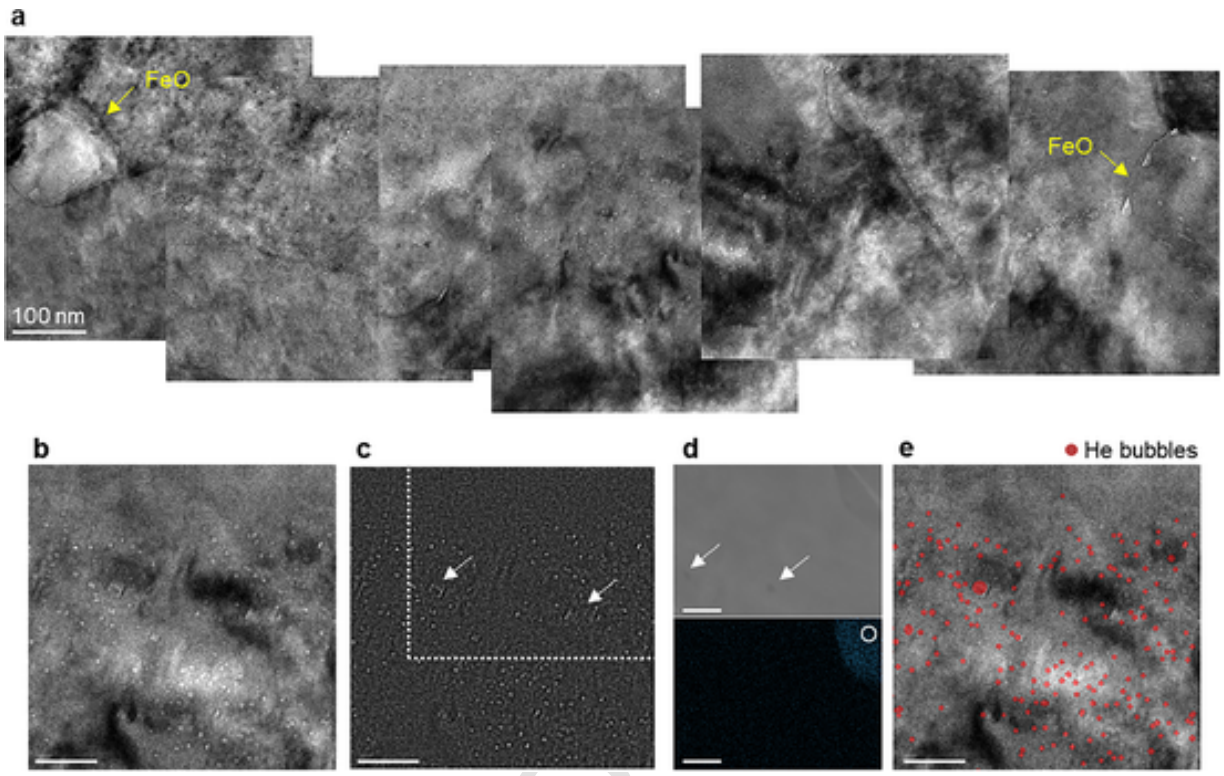

Fig. 8. Microstructural characterization of S-0 after irradiation with 5000 appm helium at 500 ˚C. (a) TEM micrographs of the peak damage region of S-0. (b) TEM micrograph showing the development of helium bubbles. (c) Preprocessed image of (b) to better visualize helium bubbles. (d) Enlarged STEM micrograph of the boxed region in (c) and corresponding STEM-EDS map. White arrows indicate the bubble-like features and the absence of oxygen signals from the STEM-EDS map. (e) TEM micrograph showing the detected helium bubbles, marked with red dots. Scale bars in (b–e), 50 nm.

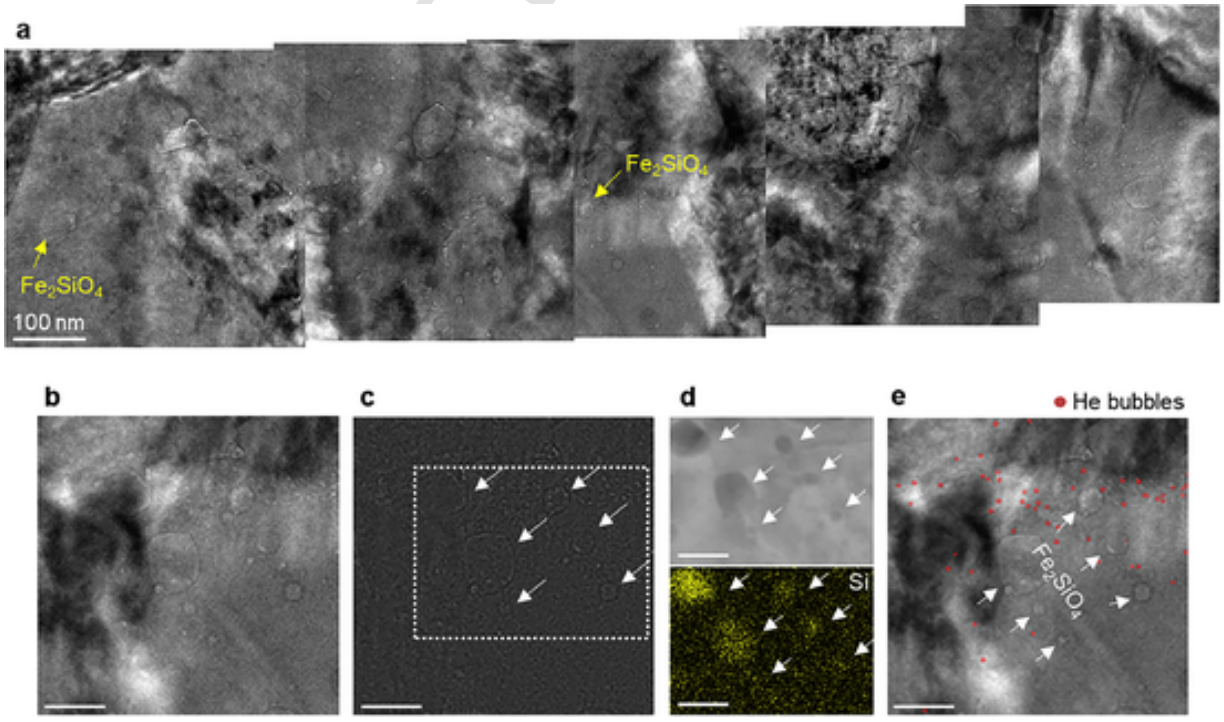

Fig. 9. Microstructural characterization of S-Fe_2SiO_4 after irradiation with 5000 appm helium at 500 ˚C. (a) TEM micrographs of the peak damage region of S-Fe_2SiO_4. (b) TEM micrograph showing the development of helium bubbles. (c) Preprocessed image of (b) to better visualize helium bubbles. (d) Enlarged STEM micrograph of the boxed region in (c) and corresponding STEM-EDS map. White arrows indicate bubble-like features and the presence of silicon signals in the STEM-EDS map. (e) TEM micrograph showing the detected helium bubbles, marked with red dots. Scale bars in (b–e), 50 nm.

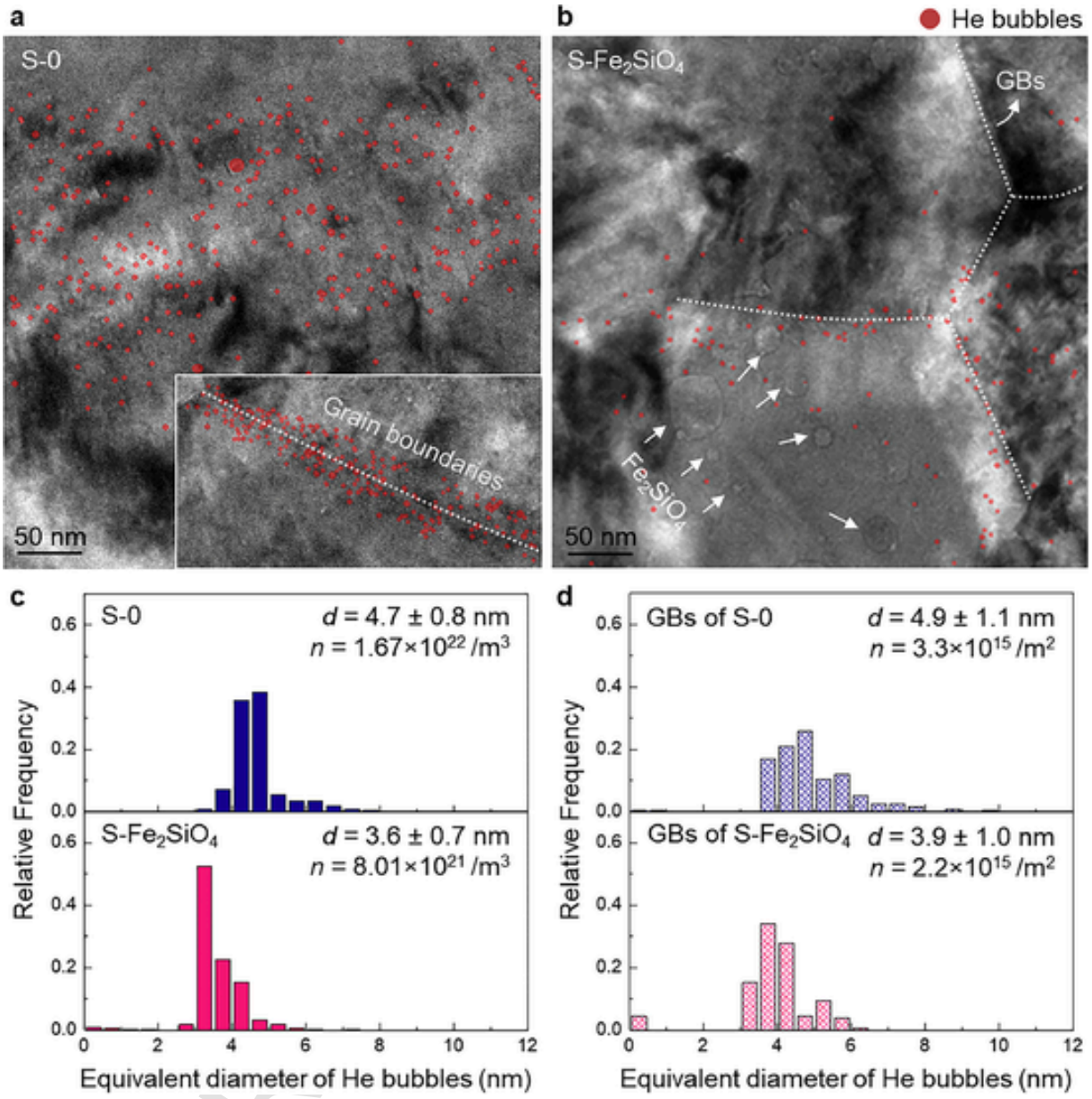

Fig. 10. Development of helium bubbles upon irradiation with 5000 appm helium at 500 °C. (a,b) TEM micrographs of the peak damage regions in (a) S-0 and (b) S-Fe_2SiO_4. Helium bubbles are highlighted in red and white dotted lines indicate grain boundaries. (c,d) Relative frequency of helium bubbles as a function of equivalent diameter in (c) the whole matrix of S-0 and S-Fe_2SiO_4 and (d) the grain boundaries of S-0 and S-Fe_2SiO_4. *d* and *n* are the average diameter and the number density of helium bubbles, respectively.

large number of helium bubbles were found, and a few bubbles were on the verge of coalescing with neighboring bubbles. On the other hand, in S-Fe_2SiO_4 (Fig. 10b), both the size and the number of bubbles detected were smaller compared to S-0; Fe_2SiO_4 nanoparticles with diameters in the range of a few tens of nanometers were additionally observed, and some of the bubbles were found at the interface between oxide nanoparticles and the Fe matrix. Moreover, being rather sparsely distributed, most of the gas bubbles were sufficiently far apart, thereby their coalescence remaining less likely compared to bubbles in S-0.

The quantitative analysis of the size distribution and number density of helium bubbles provides further support for the delayed development of critical helium damage. Fig. 10c,d display the size distribution of the observed helium bubbles characterized by the equivalent diameter. Fig. 10c shows those from the whole matrix of S-0 and S-Fe_2SiO_4, respectively, while Fig. 10d shows those from the GBs of the samples. In all cases, the histograms of S-Fe_2SiO_4 shifted towards a smaller size regime compared to S-0, indicating the suppressed growth of helium gas bubbles. Specifically, when comparing the total helium bubbles observed in S-Fe_2SiO_4 against S-0, the average diameter (*d*) and the number density (*n*) of helium bubbles in the peak damage region decreased by 23 % and 51 %, respectively. In this region, the maximum concentration of helium was 5000 appm, which is well above the typical level required for a civilian fusion power reactor. The difference decreased slightly when comparing helium bubbles at GBs, but still, the *d* and *n* were smaller by 22 % and 30 % in S-Fe_2SiO_4 than in S-0. This reduction in helium bubble size is expected to reduce materials' susceptibility to embrittlement, considering that damage and fracture tend to follow extreme-value statistics in the cavity size distribution. That said, one should note that the actual effectiveness of such helide formers in mitigating helium embrittlement necessitates further investigation, including microstructure optimization and mechanical testing, given that ma-

terials' resistance to helium embrittlement is dependent on the weakest grain boundaries.

3.4. Practical implications

In order for fusion power reactors to be practical, fusion structural materials should be capable of withstanding helium concentration of ~1000–2000 appm (0.1–0.2 at%). If a helide former can absorb one helium atom per molecule, incorporating 0.1–0.2 mol% of helide formers has the potential to absorb the majority of helium present in the matrix. When considering molar volumes, including 0.1–0.2 mol% of Fe_2SiO_4 corresponds to ~0.6–1.2 vol%. This volume fraction is within the upper limit of 2 vol%, which is generally imposed due to the reduction in tensile elongation with increasing volume fraction of nanodispersoids. Therefore, it is expected that improved helium tolerance and acceptable toughness can simultaneously be achieved by adopting helide formers.

The uptake capacity and molar volume of helide formers may vary. However, considering that nano-phases with low $\mathscr{E}_{emb}$ identified in Ref. [4] tend to have greater r_{max} (> 1.5 Å) than Fe_2SiO_4, a smaller volume fraction of such nano-phases may be sufficient to absorb all the helium atoms provided that the particle spacing is adequately small. For instance, fayalite Fe_2SiO_4 used in this study was chosen for demonstration purposes and has moderate r_{max} (1.15 Å) and $\mathscr{E}_{emb}$ (0.65 eV), as compared to phases such as SiO_2, which has a larger r_{max} of 1.93 Å and a lower $\mathscr{E}_{emb}$ of 0.1 eV. In addition, such phases often have a crystal structure with higher porosity and more interconnected internal free volume than those of Fe_2SiO_4. Moreover, the phase boundaries between nano-phases and the metal matrix can also serve as helium sinks, further reducing the required volume fraction of helide formers. Thus, the volume fraction of nano-phases needed for helium storage capacity could theoretically be even smaller than 0.6 vol%.

That said, there is a lower limit to consider, as the nano-phases need to be spatially distributed uniformly when viewed at a 10^2 nm length scale, which should be smaller than the size of the matrix grains. Inter-particle spacing (l) can be calculated using the particle radius (r) and volume fraction (V_f) as follows: $l = r\sqrt{\pi/V_f}$. If we assume $l = 250$ nm and $r = 14$ nm, which are the half the size of the matrix grains of S-Fe_2SiO_4 and the average radius of Fe_2SiO_4, V_f becomes ~0.99%. It is thus expected that 1–2 vol% of Fe_2SiO_4 (or other nano-phases) is required to ensure comprehensive protection against helium segregation and potential damage across all regions of the GBs.

Furthermore, it is of crucial importance to refine the nano-phases through further structural optimization. When the chemical potential of helium within the interface fluid-gas phase becomes lower than that within the bulk lattice of the nano-phases, interface bubbles being to nucleate and grow, while the nano-phases effectively serve as "helium storage tanks" for filling these bubbles [18,49]. While low-dimensional openings are less detrimental in terms of crack evolution when compared to 2D openings [4,5], there is still a potential risk as large bubbles can readily transition into expanding voids, which may subsequently induce swelling [13]. Therefore, the nano-phases should preferably be on the order of a few nanometers like nano-oxides in NODS, to ensure that the bubbles remain suitably small.

In addition to helium-absorbing capability, there are other important considerations that warrant further investigation, such as the interference effects from hydrogen and/or tritium and the radiation stability of these nano-phases. First, in real applications, not only helium but also other transmutation gasses, such as hydrogen, are produced, and the material is subject to hydrogen/tritium permeation [1]. Large atomic-scale free volume could be attractive to such gaseous species as well, and thus site competition and selectivity should be further explored and assessed.

Second, various types of defects can be generated under neutron irradiation, including vacancies and self-interstitials, which can result in structural deterioration and chemical changes in nano-phases [50]. At relatively low temperatures, where vacancies and self-interstitials are slow to be annihilated, excess defects can induce mechanical instability, leading to a transition from crystalline to amorphous structures [50,51]. The susceptibility of a ceramic phase to amorphization is often correlated with the energy required to disrupt the structure, but this dependence can be either negative or positive, depending on the crystal structures [52–54]. For example, fluorite derivatives, characterized by metal sublattices that are fully dense without constitutional vacancies, exhibit greater resistance to amorphization when the stored energy due to point-defect accumulation is low and the extent of the chemically disordered phase in the phase diagram is significant [53]. In contrast, spinel phases [52], which possess inherent structural vacancies on the cation sublattice, or some complex silicates like the Al_2O_3–MgO-SiO_2 system [54] display an opposing trend; amorphization resistance improves as the energy required to disorder the structure increases. The extent to which these relationships apply to the radiation stability of different classes of complex ceramic phases requires further investigation.

Moreover, among several silicates, which tend to have a large atomic-scale free volume, "simpler" phases with a smaller number of distinct cation sites and a smaller number of different atom types were found to be more amorphization-resistant [55,56]. Also, for olivine phases like $(Fe, Mg)_2SiO_4$, used in this work, a correlation has been reported between amorphization resistance and bond ionicity, with a focus on the directionality of bonds [55,57], aligning well with studies on the amorphization resistance of various simple materials, such as Si, Ge, and SiC [58]. These findings suggest the possibility of modifying amorphization resistance through composition optimization.

On the other hand, vacancy diffusion is accelerated under irradiation at high temperatures. While amorphization may not necessarily occur (in fact, the more susceptible to amorphization, the higher the critical amorphization temperature [52]), the size of the atomic-scale free volume remains subject to change especially at later stages of irradiation due to processes like radiation knock-out and thermal activation [4]. That said, if the evolved helium bubbles remain within a nano-phase, characterized by 0D openings, they cause less harm in comparison to helium accumulating at 2D grain boundaries [4]. Composite materials with such helium-absorbing nano-phases would thus likely exhibit greater helium tolerance, even if the size of the atomic-scale free volume is eventually disrupted [4].

Lastly, our results demonstrate that the approach of comparing experimental XRD patterns with computed XRD patterns could be advantageous in detecting foreign elements incorporated into bulk lattices. Therefore, we expect that the approach presented in this work can provide an effective means to study the presence and position of foreign elements, even when no significant change in interplanar spacing is apparent. Such investigation could contribute to a deeper understanding of the effects of foreign elements on various properties of materials in both fusion and other relevant fields.

4. Conclusions

Structural analysis using a combination of *ab initio* calculations and GIXRD experimentally demonstrated that nano-heterophases with atomic-scale free volume such as Fe_2SiO_4 can absorb and store helium not only at the nano-phase boundary but also in its lattice, forming a helide compound Fe_2SiO_4·He. The results suggest that helium atoms can be distributed over the atomic-scale free volume inside the crystal lattice, rather than being aggregated in a few local free volumes. Such helide formers may allow for helium storage of > ~10 at% locally, which means that 1–2 vol% of helide formers could be enough to sequester a majority of the helium produced throughout the service life of fusion structural materials (projected based on the dpa limit) away from the polycrystal grain boundaries, and hence potentially mitigate helium embrittlement. Indeed, the inclusion of just 1 vol% of helium-absorbing

nano-heterophases resulted in an overall reduction of approximately > 20 % in the diameter and > 50 % in the number density of helium bubbles in the peak damage region in helium ion radiation experiment at 500 °C. Although some helium bubbles were still present at the GBs, the maximum diameter was smaller by 30 %. The approach of incorporating helide formers is generic and can be applied to any polycrystalline fusion structural materials, since the difference in $\mathscr{E}_{emb}$ is significant. Finding easy-to-disperse helide formers and estimating their full helium-absorbing capacity would accelerate the optimal design of helium-tolerant composite materials for fusion.

Declaration of competing interest

The authors declare that there are no competing interests.

Data availability

The data that support the findings of this study are available from the corresponding author at liju@mit.edu upon reasonable request.

Acknowledgments

This work was supported by Eni S.p.A. through the MIT Energy Initiative. S.Y.K. gratefully acknowledges partial financial support from the Kwanjeong Scholarship. M.J.L and E.S.P were supported by the Creative Materials Discovery Program through the National Research Foundation of Korea (NRF) funded by the Korean Government (MSIT) (no. NRF-2019M3D1A1079215). The Texas Advanced Computing Center provided computing resources for the calculations in this work. The authors acknowledge the support of the 5A-XRS beamline at the Pohang Light Source, Pohang Accelerator Laboratory, and the 11–1D-C beamline at the Advanced Photon Source, Argonne National Laboratory. The authors thank Ms. Ji Eun Lee for her assistance in GIXRD experiments, and Dr. Austin Akey, Dr. Yi-Sheng Chen, Dr. Ranming Niu, and Prof. Julie Cairney for their valuable discussions.

Supplementary materials

Supplementary material associated with this article can be found, in the online version, at doi:10.1016/j.actamat.2024.119654.

References

[1] J. Knaster, A. Moeslang, T. Muroga, Materials research for fusion, Nat. Phys. 12 (2016) 424–434, https://doi.org/10.1038/NPHYS3735.
[2] S.J. Zinkle, J.T. Busby, Structural materials for fission & fusion energy, Mater. Today. 12 (2009) 12–19, https://doi.org/10.1016/S1369-7021(09)70294-9.
[3] A. Molvik, A. Ivanov, G.L. Kulcinski, D. Ryutov, J. Santarius, T. Simonen, B.D. Wirth, A. Ying, A gas dynamic trap neutron source for fusion material and subcomponent testing, Fusion Sci. Technol. 57 (2010) 369–394, https://doi.org/10.13182/FST10-A9499.
[4] H. Xu, S.Y. Kim, D. Chen, G.B. Olson, C. Sun, J. Li, Materials genomics search of possible helium-absorbing nano-phases in fusion structural materials, Adv. Sci. 9 (2022) 2203555.
[5] F.R.N. Nabarro, The influence of elastic strain on the shape of particles segregating in an alloy, Proc. Phys. Soc. 52 (1940) 90–93.
[6] M.R. Gilbert, S.L. Dudarev, D. Nguyen-Manh, S. Zheng, L.W. Packer, J.C. Sublet, Neutron-induced dpa, transmutations, gas production, and helium embrittlement of fusion materials, J. Nucl. Mater. 442 (2013) S755–S760, https://doi.org/10.1016/j.jnucmat.2013.03.085.
[7] K.P. So, X. Liu, H. Mori, A. Kushima, J.G. Park, H.S. Kim, S. Ogata, Y.H. Lee, J. Li, Ton-scale metal–carbon nanotube composite: the mechanism of strengthening while retaining tensile ductility, Extrem. Mech. Lett. 8 (2016) 245–250, https://doi.org/10.1016/j.eml.2016.04.002.
[8] K.P. So, A. Kushima, J.G. Park, X. Liu, D.H. Keum, H.Y. Jeong, F. Yao, S.H. Joo, H.S. Kim, H. Kim, J. Li, Y.H. Lee, Intragranular dispersion of carbon nanotubes comprehensively improves aluminum alloys, Adv. Sci. 5 (2018) 1800115, https://doi.org/10.1002/advs.201800115.
[9] K.P. So, D. Chen, A. Kushima, M. Li, S. Kim, Y. Yang, Z. Wang, J.G. Park, Y.H. Lee, R.I. Gonzalez, M. Kiwi, E.M. Bringa, L. Shao, J. Li, Dispersion of carbon nanotubes in aluminum improves radiation resistance, Nano Energy 22 (2016) 319–327, https://doi.org/10.1016/j.nanoen.2016.01.019.
[10] P. Cao, K.P. So, Y. Yang, J.G. Park, M. Li, L. Yan, J. Hu, M. Kirk, M. Li, Y.H. Lee, M.P. Short, J. Li, Carbon nanotube (CNT) metal composites exhibit greatly reduced radiation damage, Acta Mater 203 (2021) 116483, https://doi.org/10.1016/j.actamat.2020.116483.
[11] C.M. Parish, K.A. Unocic, L. Tan, S.J. Zinkle, S. Kondo, L.L. Snead, D.T. Hoelzer, Y. Katoh, Helium sequestration at nanoparticle-matrix interfaces in helium + heavy ion irradiated nanostructured ferritic alloys, J. Nucl. Mater. 483 (2017) 21–34, https://doi.org/10.1016/j.jnucmat.2016.10.038.
[12] Y.R. Lin, W.Y. Chen, L. Tan, D.T. Hoelzer, Z. Yan, C.Y. Hsieh, C.W. Huang, S.J. Zinkle, Bubble formation in helium-implanted nanostructured ferritic alloys at elevated temperatures, Acta Mater 217 (2021) 117165, https://doi.org/10.1016/j.actamat.2021.117165.
[13] G.R. Odette, Recent progress in developing and qualifying nanostructured ferritic alloys for advanced fission and fusion applications, Jom 66 (2014) 2427–2441, https://doi.org/10.1007/s11837-014-1207-5.
[14] G. Robert Odette, N.J. Cunningham, T. Stan, M. Ershadul Alam, Y. De Carlan, Nano-oxide Dispersion-Strengthened Steels, Elsevier Inc., 2019, https://doi.org/10.1016/B978-0-12-397046-6.00012-5.
[15] G.R. Odette, On the status and prospects for nanostructured ferritic alloys for nuclear fission and fusion application with emphasis on the underlying science, Scr. Mater. 143 (2018) 142–148, https://doi.org/10.1016/j.scriptamat.2017.06.021.
[16] Y. Jin, Y. Jiang, L. Yang, G. Lan, G.Robert Odette, T. Yamamoto, J. Shang, Y. Dang, First principles assessment of helium trapping in Y2TiO5 in nano-featured ferritic alloys, J. Appl. Phys. 116 (2014), https://doi.org/10.1063/1.4897503.
[17] L. Yang, Y. Jiang, G.Robert Odette, T. Yamamoto, Z. Liu, Y. Liu, Trapping helium in Y2Ti2O7 compared to in matrix iron: a first principles study, J. Appl. Phys. 115 (2014), https://doi.org/10.1063/1.4871282.
[18] L. Yang, Y. Jiang, Y. Wu, G.R. Odette, Z. Zhou, Z. Lu, The ferrite/oxide interface and helium management in nano-structured ferritic alloys from the first principles, Acta Mater 103 (2016) 474–482, https://doi.org/10.1016/j.actamat.2015.10.031.
[19] L. Tan, L.L. Snead, Y. Katoh, Development of new generation reduced activation ferritic-martensitic steels for advanced fusion reactors, J. Nucl. Mater. 478 (2016) 42–49, https://doi.org/10.1016/j.jnucmat.2016.05.037.
[20] W.F. Kuhs, T.C. Hansen, A. Falenty, Filling ices with helium and the formation of helium clathrate hydrate, J. Phys. Chem. Lett. 9 (2018) 3194–3198, https://doi.org/10.1021/acs.jpclett.8b01423.
[21] P. Teeratchanan, A. Hermann, Computational phase diagrams of noble gas hydrates under pressure, J. Chem. Phys. 143 (2015), https://doi.org/10.1063/1.4933371.
[22] S.A. Bourne, M.R. Caira, Inclusion Compounds, in: ullmann's, Encycl. Ind. Chem. (2014) 1–20, https://doi.org/10.1002/14356007.a14_119.pub2.
[23] X. Dong, A.R. Oganov, A.F. Goncharov, E. Stavrou, S. Lobanov, G. Saleh, G.R. Qian, Q. Zhu, C. Gatti, V.L. Deringer, R. Dronskowski, X.F. Zhou, V.B. Prakapenka, Z. Konôpková, I.A. Popov, A.I. Boldyrev, H.T. Wang, A stable compound of helium and sodium at high pressure, Nat. Chem. 9 (2017) 440–445, https://doi.org/10.1038/nchem.2716.
[24] X. Wang, C. Hatzoglou, B. Sneed, Z. Fan, W. Guo, K. Jin, D. Chen, H. Bei, Y. Wang, W.J. Weber, Y. Zhang, B. Gault, K.L. More, F. Vurpillot, J.D. Poplawsky, Interpreting nanovoids in atom probe tomography data for accurate local compositional measurements, Nat. Commun. 11 (2020) 1–11, https://doi.org/10.1038/s41467-020-14832-w.
[25] J.E. Schmidt, L. Peng, J.D. Poplawsky, B.M. Weckhuysen, Nanoscale chemical imaging of zeolites using atom probe tomography, Angew. Chemie - Int. Ed. 57 (2018) 10422–10435, https://doi.org/10.1002/anie.201712952.
[26] Y.S. Chen, D. Haley, S.S.A. Gerstl, A.J. London, F. Sweeney, R.A. Wepf, W.M. Rainforth, P.A.J. Bagot, M.P. Moody, Direct observation of individual hydrogen atoms at trapping sites in a ferritic steel, Science (80-.) 355 (2017) 1196–1199, https://doi.org/10.1126/science.aal2418.
[27] A.J. Lloyd, B.R. Hester, S.J. Baxter, S. Ma, V.B. Prakapenka, S.N. Tkachev, C. Park, A.P. Wilkinson, Hybrid double perovskite containing helium: [He2][CaZr]F6, Chem. Mater. 33 (2021) 3132–3138, https://doi.org/10.1021/acs.chemmater.0c04782.
[28] J.A. Sans, F.J. Manjón, C. Popescu, V.P. Cuenca-Gotor, O. Gomis, A. Muñoz, P. Rodríguez-Hernández, J. Contreras-García, J. Pellicer-Porres, A.L.J. Pereira, D. Santamaría-Pérez, A. Segura, Ordered helium trapping and bonding in compressed arsenolite: synthesis of As4O6·2He, Phys. Rev. B. 93 (2016) 3–7, https://doi.org/10.1103/PhysRevB.93.054102.
[29] T. Sato, H. Takada, T. Yagi, H. Gotou, T. Okada, D. Wakabayashi, N. Funamori, Anomalous behavior of cristobalite in helium under high pressure, Phys. Chem. Miner. 40 (2013) 3–10, https://doi.org/10.1007/s00269-012-0540-x.
[30] G. Shen, Q. Mei, V.B. Prakapenka, P. Lazor, S. Sinogeikin, Y. Meng, C. Park, Effect of helium on structure and compression behavior of SiO2 glass, Proc. Natl. Acad. Sci. U. S. A. 108 (2011) 6004–6007, https://doi.org/10.1073/pnas.1102361108.
[31] G. Kresse, J. Furthmüller, Efficiency of ab-initio total energy calculations for metals and semiconductors using a plane-wave basis set, Comput. Mater. Sci. 6 (1996) 15–50, https://doi.org/10.1016/0927-0256(96)00008-0.
[32] W. Kohn, L.J. Sham, Self-consistent equations including exchange and correlation effects, Phys. Rev. 140 (1965) A1133–A1138, https://doi.org/10.1103/PhysRev.140.A1133.
[33] P. Hohenberg, W. Kohn, Inhomogeneous electron gas, Phys. Rev. 136 (1964) B864–B871, https://doi.org/10.1103/PhysRev.136.B864.
[34] A. Jain, S.P. Ong, G. Hautier, W. Chen, W.D. Richards, S. Dacek, S. Cholia, D. Gunter, D. Skinner, G. Ceder, K.A. Persson, The Materials Project: a materials genome approach to accelerating materials innovation, APL Mater 1 (2013) 11002.
[35] A.L. Spek, Single-crystal structure validation with the program PLATON, J. Appl. Crystallogr. 36 (2003) 7–13, https://doi.org/10.1107/S0021889802022112.

[36] J.P. Perdew, K. Burke, M. Ernzerhof, Generalized gradient approximation made simple, Phys. Rev. Lett. 77 (1996) 3865–3868, https://doi.org/10.1103/PhysRevLett.77.3865.
[37] P.E. Blöchl, Projector augmented-wave method, Phys. Rev. B. 50 (1994) 17953–17979, https://doi.org/10.1103/PhysRevB.50.17953.
[38] K. Momma, F. Izumi, VESTA 3 for three-dimensional visualization of crystal, volumetric and morphology data, J. Appl. Crystallogr. 44 (2011) 1272–1276.
[39] J.F. Ziegler, M.D. Ziegler, J.P. Biersack, SRIM - The stopping and range of ions in matter (2010), Nucl. Instruments Methods Phys. Res. Sect. B Beam Interact. with Mater. Atoms. 268 (2010) 1818–1823, https://doi.org/10.1016/j.nimb.2010.02.091.
[40] R.E. Stoller, M.B. Toloczko, G.S. Was, A.G. Certain, S. Dwaraknath, F.A. Garner, On the use of SRIM for computing radiation damage exposure, Nucl. Instruments Methods Phys. Res. Sect. B Beam Interact. with Mater. Atoms. 310 (2013) 75–80, https://doi.org/10.1016/j.nimb.2013.05.008.
[41] M.B. Lewis, K. Farrell, Migration behavior of helium under displacive irradiation in stainless steel, nickel, iron and zirconium, Nucl. Inst. Methods Phys. Res. B. 16 (1986) 163–170, https://doi.org/10.1016/0168-583X(86)90008-X.
[42] D.B. Williams, C.B. Carter, Electron Energy-Loss Spectrometers and Filters BT - Transmission Electron Microscopy: A Textbook for Materials Science, in: D.B. Williams, C.B. Carter (Eds.), Springer US, Boston, MA, 2009: pp. 679–698. https://doi.org/10.1007/978-0-387-76501-3_37.
[43] L. Lutterotti, S. Matthies, H.-R. Wenk, A.S. Schultz, J.W. Richardson Jr, Combined texture and structure analysis of deformed limestone from time-of-flight neutron diffraction spectra, J. Appl. Phys. 81 (1997) 594–600.
[44] L. Lutterotti, R. Vasin, H.R. Wenk, Rietveld texture analysis from synchrotron diffraction images. I. Calibration and basic analysis, Powder Diffr 29 (2014) 76–84, https://doi.org/10.1017/S0885715613001346.
[45] D.G. Henshaw, Structure of solid helium by neutron diffraction, Phys. Rev. 109 (1958) 328–330, https://doi.org/10.1103/PhysRev.109.328.
[46] T. Yagi, E. Iida, H. Hirai, N. Miyajima, T. Kikegawa, M. Bunno, High-pressure behavior of a SiO2 clathrate observed by using various pressure media, Phys. Rev. B - Condens. Matter Mater. Phys. 75 (2007) 1–6, https://doi.org/10.1103/PhysRevB.75.174115.
[47] P.A. Guńka, K.F. Dziubek, A. Gładysiak, M. Dranka, J. Piechota, M. Hanfland, A. Katrusiak, J. Zachara, Compressed Arsenolite As4O6 and Its Helium Clathrate As4O6·2He, Cryst. Growth Des. 15 (2015) 3740–3745, https://doi.org/10.1021/acs.cgd.5b00390.
[48] M.R. Rafiuddin, A.P. Grosvenor, Probing the effect of radiation damage on the structure of rare-earth phosphates, J. Alloys Compd. 653 (2015) 279–289, https://doi.org/10.1016/j.jallcom.2015.08.276.
[49] T. Stan, Y. Wu, J. Ciston, T. Yamamoto, G.R. Odette, Characterization of polyhedral nano-oxides and helium bubbles in an annealed nanostructured ferritic alloy, Acta Mater 183 (2020) 484–492, https://doi.org/10.1016/j.actamat.2019.10.045.
[50] A. Bhattacharya, S.J. Zinkle, J. Henry, S.M. Levine, P.D. Edmondson, M.R. Gilbert, H. Tanigawa, C.E. Kessel, Irradiation damage concurrent challenges with RAFM and ODS steels for fusion reactor first-wall/blanket: a review, JPhys. Energy 4 (2022), https://doi.org/10.1088/2515-7655/ac6f7f.
[51] C. Jiang, M.J. Zheng, D. Morgan, I. Szlufarska, Amorphization driven by defect-induced mechanical instability, Phys. Rev. Lett. 111 (2013) 1–5, https://doi.org/10.1103/PhysRevLett.111.155501.
[52] B.P. Uberuaga, M. Tang, C. Jiang, J.A. Valdez, R. Smith, Y. Wang, K.E. Sickafus, Opposite correlations between cation disordering and amorphization resistance in spinels versus pyrochlores, Nat. Commun. 6 (2015), https://doi.org/10.1038/ncomms9750.
[53] K.E. Sickafus, R.W. Grimes, J.A. Valdez, A. Cleave, M. Tang, M. Ishimaru, S.M. Corish, C.R. Stanek, B.P. Uberuaga, Radiation-induced amorphization resistance and radiation tolerance in structurally related oxides, Nat. Mater. 6 (2007) 217–223, https://doi.org/10.1038/nmat1842.
[54] L.M. Wang, S.X. Wang, W.L. Gong, R.C. Ewing, W.J. Weber, Amorphization of ceramic materials by ion beam irradiation, Mater. Sci. Eng. A. 253 (1998) 106–113, https://doi.org/10.1016/s0921-5093(98)00715-1.
[55] L.M. Wang, R.C. Ewing, Amorphization of complex ceramic materials — minerals, MRS Bull. 17 (1992) 38–44.
[56] L.M. Wang, R.K. Eby, J. Janeczek, R.C. Ewing, In situ TEM study of ion-beam-induced amorphization of complex silicate structures, Nucl. Inst. Methods Phys. Res. B. 59–60 (1991) 395–400, https://doi.org/10.1016/0168-583X(91)95245-9.
[57] G.S. Was, L.E. Rehn, D.M. Follstaedt, in: Proceedings of the phase formation and modification by beam-solid interactions, Materials Research Society, Pittsburgh, PA (United States), 1992.
[58] H.M. Naguib, R. Kelly, Criteria for bombardment-induced structural changes in non-metallic solids, Radiat. Eff. 25 (1975) 1–12, https://doi.org/10.1080/00337577508242047.